

Flexible and Ultrasoft Inorganic 1D Semiconductor and Heterostructure Systems Based on SnIP

Claudia Ott, Felix Reiter, Maximilian Baumgartner, Markus Pielmeier, Anna Vogel, Patrick Walke, Stefan Burger, Michael Ehrenreich, Gregor Kieslich, Dominik Daisenberger, Jeff Armstrong, Ujwal Kumar Thakur, Pawan Kumar, Shunda Chen, Davide Donadio, Lisa S. Walter, R. Thomas Weitz, Karthik Shankar,* and Tom Nilges**

Low dimensionality and high flexibility are key demands for flexible electronic semiconductor devices. SnIP, the first atomic-scale double helical semiconductor combines structural anisotropy and robustness with exceptional electronic properties. The benefit of the double helix, combined with a diverse structure on the nanoscale, ranging from strong covalent bonding to weak van der Waals interactions, and the large structure and property anisotropy offer substantial potential for applications in energy conversion and water splitting. It represents the next logical step in downscaling the inorganic semiconductors from classical 3D systems, via 2D semiconductors like MXenes or transition metal dichalcogenides, to the first downsizeable, polymer-like atomic-scale 1D semiconductor SnIP. SnIP shows intriguing mechanical properties featuring a bulk modulus three times lower than any IV, III-V, or II-VI semiconductor. In situ bending tests substantiate that pure SnIP fibers can be bent without an effect on their bonding properties. Organic and inorganic hybrids are prepared illustrating that SnIP is a candidate to fabricate flexible 1D composites for energy conversion and water splitting applications. SnIP@C₃N₄ hybrid forms an unusual soft material core-shell topology with graphenic carbon nitride wrapping around SnIP. A 1D van der Waals heterostructure is formed capable of performing effective water splitting.

1. Introduction

The development of semiconductors for electronic devices is driven by the need of miniaturization, increasing efficiency, flexibility, and stability. Therefore, classical IV, III-V, or II-VI 3D semiconductors are fabricated in nanoparticulate form and applied for instance as quantum dots in numerous electronic devices.^[1,2] The reduction of size leads to fundamental changes in the optical and electronic properties. Electronic excitations shift to higher energy, and the oscillator strength is concentrated into a few transitions. As a consequence of quantum confinement properties like bandgaps, melting points, or phase transition temperatures are tuned. If one focusses on the density of states (DOS) in semiconductor nanostructures with different dimensionality going from 3D toward 1D and 0D, an increasing texturing of the DOS leading to discrete energy levels in low-dimensional systems

Dr. C. Ott, F. Reiter, Dr. M. Baumgartner, M. Pielmeier, A. Vogel,
P. Walke, Prof. T. Nilges

Department of Chemistry
Synthesis and Characterization of Innovative Materials group
Technical University of Munich
Lichtenbergstrasse 4, 85748 Garching, Germany
E-mail: tom.nilges@lrz.tum.de

S. Burger, M. Ehrenreich, Dr. G. Kieslich
Department of Chemistry
Crystal Chemistry of Functional Materials group
Technical University of Munich
Lichtenbergstrasse 4, 85748 Garching, Germany
E-mail: gregor.kieslich@tum.de

Dr. D. Daisenberger
Diamond Light Source Ltd
Harwell Science & Innovation Campus, Didcot OX11 0DE, UK

Dr. J. Armstrong
ISIS Facility
STFC Rutherford Appleton Laboratory
Didcot OX11 0QX, UK

 The ORCID identification number(s) for the author(s) of this article can be found under <https://doi.org/10.1002/adfm.201900233>.

U. K. Thakur, Dr. P. Kumar, Prof. K. Shankar
Department of Electrical and Computer Engineering
University of Alberta
11-384 Donadeo Innovation Centre For Engineering, Edmonton T6G
1H9, Canada

E-mail: kshankar@ualberta.ca
Dr. S. Chen, Prof. D. Donadio
Department of Chemistry
University of California, Davis
One Shields Avenue, Davis 95616, CA, USA

L. S. Walter, Prof. R. T. Weitz
Physics of Nanosystems
Department of Physics
Ludwig-Maximilians-University Munich
Amalienstrasse 54, 80799 Munich, Germany

Prof. R. T. Weitz
Center for NanoScience (CeNS) and Nanosystems Initiative
Munich (NIM)
Schellingstrasse 4, 80799 Munich, Germany

DOI: 10.1002/adfm.201900233

can be observed.^[1] Therefore, a consequent way of development in semiconductor science was to decrease the dimensionality and 2D systems like MXenes (graphene, phosphorene, silicene, and others) or transition metal dichalcogenides (TMD) emerged.^[3–6] Here, the layered structure introduced a feature that was not easy to achieve with bulk phase 3D semiconductors namely, morphological (graphene and TMDs) and in some cases structural (phosphorene and silicene) anisotropy. Such systems also offer enhanced flexibility alongside with electronic properties emerging from quantum confinement, and they can be easily prepared and used as monolayer materials.

The reduction in dimensionality resulted in enhanced electron–electron interactions, which for instance results in giant bandgap renormalization excitonic effects, Dirac cones, topological states, and charge density waves as shown for TMDs.^[7,8] Besides graphene, lacking of a bandgap, many other 2D materials like phosphorene or TMDs are semiconductors and can be applied in high-performance electronic devices. Field effect transistors have been made in 2014 with phosphorene^[9] and in 2015 with silicene.^[10] Another interesting but nonclassical 2D semiconductor with intriguing mechanical properties is α -Ag₂S.^[11] This material offers a metal-like ductility due to weak van der Waals interactions within structure subunits and a fluent and highly dynamic change in bonding between Ag and S atoms.

A further exciting evolution step toward an optimized performance and oxidation stability (or less-pronounced air sensitivity) was the combination of semiconductors like 2D materials to so-called van der Waals heterostructures.^[12] Different 2D materials are connected by weak van der Waals interactions to generate heterostructures with unusual properties and exciting phenomena. Promising results are reported for instance for perovskite-type, lead iodide based thin film systems where a strong relationship between the photoexcitation dynamics and morphologies of the thin films was observed.^[13] As shown recently, new preparation methods like autoperforation emerged which allows an effective production of 2D heterostructures with remarkable chemical and mechanical stability also making a large scale production possible.^[14]

The consequent next evolution step was to further reduce dimensionality to 1D-semiconductor systems. Element and compound nanowire materials have been developed in the past years which offer an increased surface area and flexibility compared with 2D systems. If fabricated in almost atomic diameters,^[15–17] either as freestanding, oriented, or randomly arranged systems, they offer enhanced flexibility and larger specific surface than the 2D counterparts. Here we report on selected physical properties of pure SnIP and SnIP heterostructure systems. Various organic polymers frequently used in batteries, solar cells, and thermoelectric applications, or C₃N₄ were successfully used to form heterostructures with SnIP. In the case of SnIP@C₃N₄ heterostructures, a remarkable photoelectrochemical stability and spontaneous core–shell segregation were observed which illustrates the potential of double helical SnIP as a defined 1D material for semiconductor applications. In the SnIP@C₃N₄ composites or heterostructures, the self-organization of C₃N₄ wrapped around SnIP due to van der Waals interactions is an example of polymer-like behavior while the photoelectrochemical performance is contingent to the semiconducting behavior of SnIP.

2. Results and Discussion

Recently, SnIP, representing the first inorganic, atomic-scale, double helix compound, attracted reasonable interest due to its intriguing structural, electronic, and optical properties.^[18] Two helices, a small ${}^1[P^-]$ and a larger ${}^1[SnI^+]$ helix nested the former into the latter in such a way that a double helix is formed. One left- and right-handed double helix are stacked along the crystallographic *a*-axis in a hexagonal array of rods. In Hermann–Mauguin notation, the two double helices present in SnIP with opposite chirality, a left handed M-helix or a right handed P-helix, fulfill the rod groups ${}_p 7_3 2$ and ${}_p 7_4 2$, respectively.^[19] Due to the anisotropic structural features with covalently-bonded helices and weak van der Waals-like interactions between the double-helix rods, this material can be the ideal candidate to combine the beneficial properties of two classes of materials, the electric properties of an inorganic semiconductor, and the mechanical properties of polymer-like systems. The structural anisotropy of SnIP is manifested in the pronounced needle-like morphology and gives therefore rise to interesting direction-dependent phenomena. Well-defined anisotropic physical properties are expected. First principle density functional theory (DFT) calculations were performed for the whole substance class of double helical MXP_n compounds with $M =$ group 14, $X =$ group 17, and $P_n =$ group 15 elements.^[20] Promising electron mobilities are up to 2164 cm² V⁻¹ s⁻¹ and good band level alignments of the valence and conduction band edges are for effective water splitting.^[21]

2.1. Mechanical Properties of SnIP

In the first set of experiments, we focused our interest on the mechanical properties of SnIP. The response to (hydrostatic) pressures and in turn the mechanical properties of SnIP were investigated by employing high pressure powder X-ray diffraction (HPPXRD) (Table S2-1, Supporting Information). In the first step, HPPXRD experiments were performed using a diamond anvil cell (DAC) setup to overview the behavior of SnIP in the pressure range $p =$ ambient to 4 GPa (see **Figure 1a**). During this experiment, SnIP was constantly illuminated by X-rays (energy of 25.5 keV) for more than 20 h substantiating the stability against hard X-rays. Subsequent profile fits of the PXRD data allow for extracting the cell parameters as a function of pressure. Lattice parameters are given in Table S2-1 in the Supporting Information. We observe anisotropic contraction upon the application of pressure, SnIP being more compressive within the *bc*-plane. This is in good agreement with the crystal chemistry of SnIP, in which the *bc*-plane is mainly governed by weak van der Waals interactions. Furthermore, the $V(p)$ relation indicates that SnIP is a very soft material with relatively large changes of the unit cell as function of pressure. In a second experiment, we performed HPPXRD using a low-pressure cell (LPC) to access the $V(p)$ relation at very low pressures, ensuring hydrostatic conditions during the experiment. The LPC setup is suitable for HPXRD in the pressure range $p =$ ambient to 0.4 GPa (**Figure 1a**, purple crosses), being ideal for the investigation of very soft materials.^[22]

The bulk modulus of SnIP was extracted by fitting a 3rd order Birch–Murnaghan equation of state to the $V(p)$ values in the

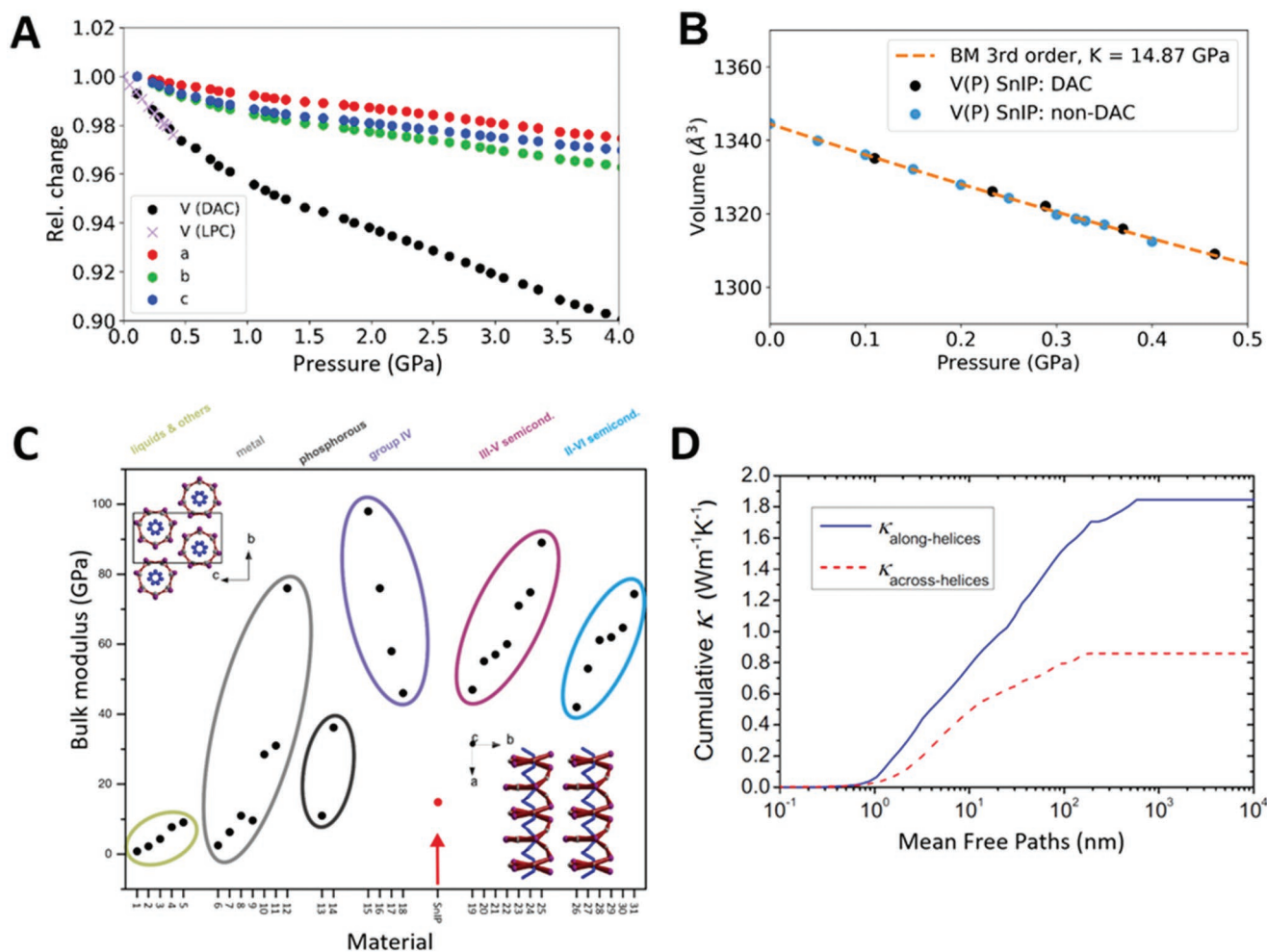


Figure 1. a) Evolution of lattice parameters and cell volumes (black from DAC; purple crosses from LPC) of SnIP up to pressures of 4 GPa. b) The bulk modulus of $K = 14.87 \pm 1.01$ GPa ($K' = 12.18$) was derived from a 3rd order Birch–Murnaghan equation of state fit given in orange. Two independent sets of cell volume measurements were performed in a diamond anvil cell (DAC) and a low pressure cell (LPC, non-DAC). c) Crystal structure sections of SnIP (insets, blue P, grey Sn, purple I) and bulk modulus of SnIP in relation to selected inorganic semiconductors, elements, and liquids. 1: methanol; 2: H₂O; 3: glycerol; 4: iodine; 5: methane hydrate; 6: Rb; 7: Na; 8: Li; 9: Ba; 10: Hg; 11: Bi; 12: Al; 13: P_{white}; 14: P_{black}; 15: Si; 16: Ge; 17: Sn; 18: Pb; 19: InSb; 20: AlSb; 21: GaSb; 22: InAs; 23: InP; 24: GaAs; 25: GaP; 26: CdTe; 27: CdSe; 28: ZnTe; 29: CdS; 30: ZnSe; 31: ZnS and d) thermal conductivity of SnIP as a function of phonon mean free path.

compiled dataset between $p =$ ambient to 0.5 GPa. We find a bulk modulus of $K = 14.87 \pm 1.01$ GPa ($K' = 12.18$; see Figure 1b and Supporting Information for details). Comparing this value with related materials with semiconducting properties like IV, III-V, or II-VI semiconductors, we find SnIP being the softest inorganic main group semiconductor currently known, see Figure 1c. The bulk modulus is three to seven times lower than such state-of-the-art semiconductors. This certainly originates from the unique bond situation, with weak van der Waals interaction within the bc -plane which facilitates a high compressibility, together with strong covalent interactions along the helices which allow a spring-like behavior and the formation of semiconducting properties.

In order to evaluate the bending properties of SnIP in more detail we investigated the Young's modulus by the aid of atomic force microscopy (AFM) in nanoindentation mode along the double helix axis [100] for wires with different diameters. We found an averaged Young's modulus in the order of 190 GPa for SnIP wires consisting of several helix strands, which is in

the same order of magnitude as silicon with 175 GPa [111], 130 GPa [100], and GaP_n [100] with P_n = N, P, and As with 191, 103, and 85 GPa, respectively.^[23] A selected measurement is given in Figure 2a. Bending SnIP along the double helix axis is obviously as hard as bending IV or III-V semiconductors in selected directions which leads to the conclusion that the covalently-bonded substructures in SnIP, the different helices and the dative ionic interaction between them (see ref. [17]) define the bending force. SnIP shows a Young's modulus along the double helix axis which is comparable to steel reported to be 180–200 GPa.^[24] The flexibility in [010] and [001] is caused by the intrinsic nature of the SnIP structure, the double helical arrangement itself, and the stacking of the double helices along the a -axis, which allows reversible bending in those directions without serious degradation. The interplay of both structural features account for the Young's modulus in those wires which seem to consist of several helix strands. Of course, due to the strong anisotropy and direction dependency of the Young's modulus on the one hand

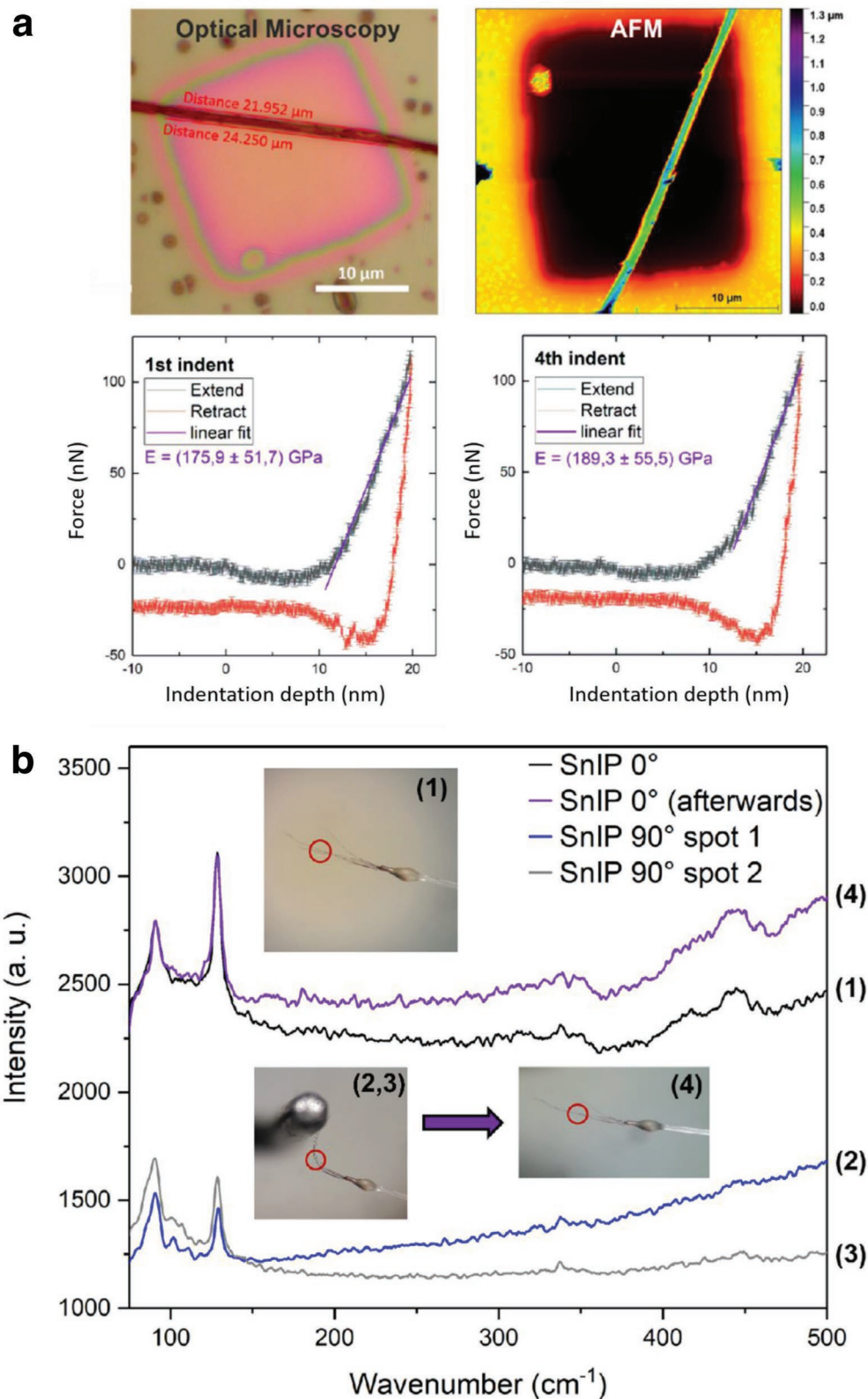


Figure 2. a) Young's Modulus determination by atomic force microscopy (AFM) measurements. Optical and AFM measurements of a suspended wire (wire 2) are shown. Two force–distance curves (Young's modulus extracted as discussed in the Supporting Information) taken in the middle of the wire. b) In situ Raman spectroscopy on SnIP upon bending. 1–4) Raman microscope measurements on red circle, without bending 1), after 90° bending, first bending 2), after second 90° bending 3) and after full relaxation 4).

and the different structures of Si and GaPn compared with SnIP on the other hand, a direct comparison of the Young's moduli can only be regarded as the first estimate for the softness of the title compound. Further details concerning the determination of the Young's modulus are given in the Supporting Information (Figures S1 and S2, Table S1-1, Supporting Information).

The question arose whether mechanical deformation (bending) of SnIP crystals will cause degradation or will have an impact on the bonding within the double helices. For van der Waals layered α -Ag₂S where it was shown that this material prevents cleavage upon bending by sliding along the (100) Ag-S slip planes (slip direction is [001]).^[11] In the case of 1D SnIP a slipping might occur in [100] parallel to the double helix strands.

Raman spectroscopy was selected as a tool to verify the influence of bending on bonding in SnIP. Quantum chemical calculations were used to assign the main Raman modes and the phonons of SnIP (see Videos and Figures S3–S5 in the Supporting Information). For both cases, spectra were recorded at room temperature and ambient pressure followed by a full assignment of the modes. In the following, the experiments are briefly discussed in detail.

According to our calculations we defined three distinct regions in the Raman spectrum, representing the interactions of the outer [SnI] helix at 120–150 cm⁻¹ (Sn-I breathing region), the inner [P] helix at 350–380 cm⁻¹ (P-P stretching region), and the interaction between the inner [P] and the outer [SnI] helix (P-P breathing region; further details see Figure S3, Supporting Information). Correlating these regions with the crystal structure and bonding situation in SnIP, the Sn-I breathing region is determined by the strong Sn-I and the weak van der Waals interactions between the double helices. Upon a so-called breathing of the outer helix the forces are determined by the intra Sn-I interactions realizing the bonding within the helix and the inter Sn-I interactions between adjacent double helix strands. According to previously reported DFT calculations^[17] the energy of this inter double helix interaction of van der Waals type is about 25 kJ mole⁻¹. The P-P stretching region is defined by the covalent P–P bonding of the inner [P]-helix. Finally, the P-P breathing region represents the dative–ionic interaction between the outer positively charged [SnI] and the inner negatively-charged [P] helix. In situ Raman spectra were performed using SnIP crystals upon bending. As shown in Figure 2b, SnIP can be bent at least up to 90° without a shift in Raman modes. Especially the strong Sn-I breathing mode at ≈129 cm⁻¹ (observed) 125 cm⁻¹ (calculated) is not affected by this mechanical deformation. This result is promising for an application of SnIP in flexible devices. We performed quantum chemical calculations to determine the influence of high-pressure on highly flexible SnIP and to evaluate the pressure-dependent structure changes. Hence, we used the cell parameters determined up to 11 GPa in a DAC cell from our pressure-dependent experiments as fixed values and optimized the internal coordinates within the framework of DFT theory and using HSE06 functionals with Grimme D2 corrections (citations see materials section). Inter double helix distances between Sn and I of neighboring double helices, representing the origin of the weak van der Waals interactions, are the most affected ones as expected from the chemical bonding situation in SnIP. Upon pressure increase, the bond distances of Sn-I within the outer helix shrink from 3.2 Å (0.1 GPa) to 3.0 Å (11.5 GPa) while the

inter double helix Sn-I distance goes down from 3.8 Å (0.1 GPa) to 3.3 Å (11.5 GPa). Nevertheless, we did not find a hint for a structural phase transition up to this pressure. All bond lengths determined for the different atom pairs are in sense full regions (see Figures S6–S8, Supporting Information).

2.2. Transport Properties of SnIP

We calculated the phonon spectra (Figure S4, Supporting Information) of SnIP with the aid of DFT and computed phonon-resolved contribution to heat transport. The thermal conductivity is in general very low, and anisotropic, with different values along ($\kappa_a = 1.8 \text{ W m}^{-1} \text{ K}^{-1}$ at room temperature) and across the helices ($\kappa_{bc} < 1 \text{ W m}^{-1} \text{ K}^{-1}$). Given the stark difference between the type of bonding along and across the helices, such small anisotropy is surprising. Across the double helices in the *bc*-plane we see a significantly lower value for the mean free paths of phonons than along the helices (See Figure 1a and the Supporting Information), indicating that there is still room for suppressing the axial component of the thermal conductivity, either by introducing defects or in composites. While van der Waals interactions account for the low value of κ_{bc} , relatively soft acoustic modes dictate the low thermal conductivity along the helices. Low values of κ may turn out interesting for both thermal insulation and thermoelectric applications.

Phonons were measured by inelastic neutron scattering (INS) and peaks were assigned relying by DFT calculations (Figure S5, Supporting Information). In good accordance with the Raman investigations we were able to distinguish between phosphorus and [SnI] phonons in the spectrum (see the Supporting Information). The phosphorus motions can be broadly broken down into concentric helical breathing and twisting modes (442, 330/265 cm⁻¹). Stretching modes along the axis of the helices occur at 339.6 cm⁻¹. The fact that these two sets of modes are comparable in frequency, yet involve spatial dimensions with varying mechanical properties indicates that the P motions are largely localized, and independent of the lateral interhelical interactions. A phonon mode of the outer Sn-I helix is localized at 99 cm⁻¹.

2.3. SnIP-Based Hybrid Materials

Encouraged by these promising results we started to evaluate if SnIP hybrids with organic polymers can be synthesized. Different polymers were chosen as the polymer part in the hybrids due to their frequent usage in various applications as devices and membranes. We examined polyethylene glycol (PEO, solid electrolyte, batteries) and polyvinyl pyrrolidone (PVP), poly(3,4-ethylenedioxythiophene)-poly(styrenesulfonate) (PEDOT/PSS, solar cells) or poly(3-hexylthiophen-2,5-diyl) (P3HT; solar cells), and fluorine/chloride doped C₃N₄ (water splitting) due to their importance for energy conversion and storage applications. In all cases, SnIP@polymer hybrids were synthesized by spin coating for thin films, and electrospinning to achieve fiber membranes. SnIP can be incorporated in all such polymers without the loss of its structural properties (see Chapter 3.1 and Figures S9–S12 in the Supporting Information) which qualifies it for a plethora of possible applications.

Another approach is to generate hybrid 1D like heterostructures of SnIP with carbon nanotubes. This was, for instance, successfully performed for elements like phosphorus^[25,26] and selenium^[27] in multiwalled carbon nanotubes. We conducted first principle DFT calculations including empirical dispersion corrections for SnIP@Carbon nanotube (CNT) heterostructures. Three different types of CNT, a metallic, semimetallic, and a semiconducting one, were selected based on their inner diameter to accommodate a single P-double helix (rod group p 7₄2) of SnIP. According to our calculations, a (10,10), (18,0), and (19,0) CNT are the most suitable candidates for the stabilization of single SnIP strands concerning simple space filling aspects of SnIP and the diameter of a given CNT (see Chapter 3.2

and Figure S13 in the Supporting Information). Once realized, such heterostructures provide access to chiral right or left-handed SnIP strands which may give rise to interesting topological quantum properties (e.g., Kramers–Weyl fermions^[28]). Single SnIP strands are highly helicoidal, if not perfectly helicoidal, and could therefore exhibit quantized electronic effects.

We investigated one promising 1D heterostructure in more detail that is the combination of SnIP with halide-doped C_3N_4 (Figure S14, Supporting Information). Fluorine and chlorine co-doped C_3N_4 (CNFCl) were used to fabricate SnIP@ C_3N_4 (F,Cl) thin-film devices for water splitting experiments (Figure 3a). A series of devices with compositions starting from 10 wt% SnIP in C_3N_4 (F,Cl) up to 90 wt% were fabricated. They

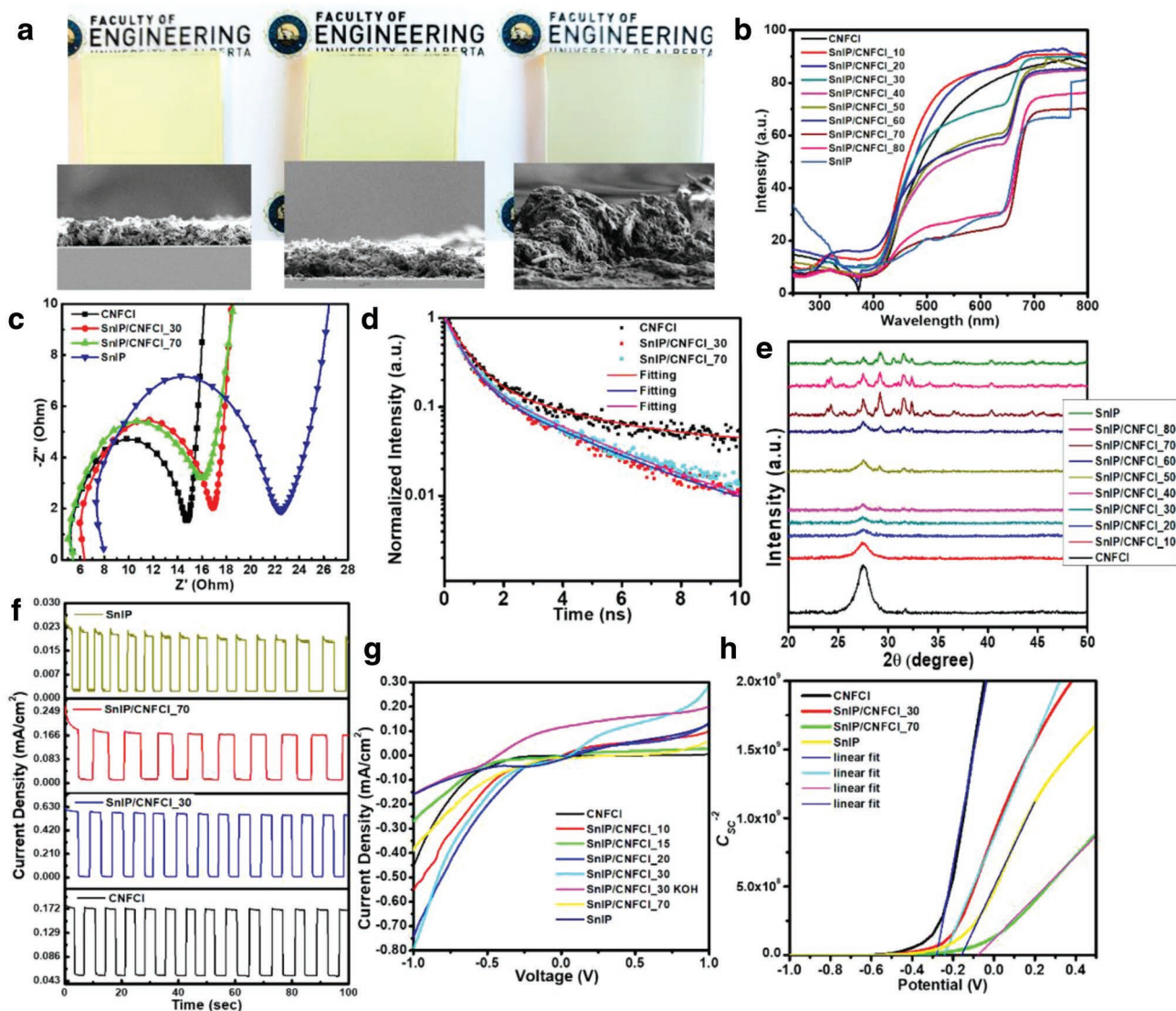


Figure 3. SnIP@ C_3N_4 (F,Cl) devices of different compositions were tested for water splitting properties. a) SnIP@ C_3N_4 (F,Cl) thin-film devices and scanning electron microscopy (SEM) pictures of bare CNFCl, SnIP/CNFCl₃₀, and SnIP/CNFCl₇₀ samples. b) UV–vis spectra of a series of SnIP@ C_3N_4 (F,Cl) devices. c) Impedance measurements of bare CNFCl, SnIP/CNFCl₃₀, SnIP/CNFCl₇₀, and SnIP devices. d) Photoluminescence lifetime measurements of bare CNFCl, SnIP/CNFCl₃₀, and SnIP/CNFCl₇₀ devices. e) Powder-XRD measurements of SnIP@ C_3N_4 (F,Cl) devices. f) Light response and current densities of bare CNFCl, bare SnIP, SnIP/CNFCl₃₀, and SnIP/CNFCl₇₀ devices. g) Current density versus potential curves for SnIP@ C_3N_4 (F,Cl) devices. h) Mott–Schottky measurements performed in 0.5 M NaSO₄ solution featuring flat band positions for SnIP, CNFCl, 30% SnIP/CNFCl, and 70% CNFCl at –0.15, –0.28, –0.24, and –0.07 V versus Ag/AgCl, respectively.

will be called SnIP/CNFCl_X with $X = 10, 20, \dots, 90$ in the following. Three representative devices are shown in Figure 3a (further details in Figure S15, Supporting Information). UV-vis spectra in Figure 3b clearly show the two distinct absorption band edges, corresponding to CNFCl at ≈ 420 nm and to SnIP at ≈ 650 nm for the different samples. The CNFCl displayed a peak at ca. 300 nm due to π - π^* transition and another peak at ca. 380 nm with an extended band tail up to 500 nm originated due to n - π^* transition. For the SnIP/CNFCl the UV-vis absorbance was strongly increased in the visible spectral region with a sharp band edge at 690 nm clearly indicating improvement of visible light absorption by SnIP/CNFCl composite. Further, the bandgap of materials was determined with the help of Tauc plots. The bandgap of CNFCl was found to be 2.41 eV, slightly lower than previously reported method for F doped g - C_3N_4 ^[29] which might be due to formation of sheets and intercalation of some chlorine. The SnIP/CNFCl composites show two band edge positions corresponded to CNFCl and SnIP at 2.39 and 1.70 eV respectively. For higher SnIP content, the band edge is red-shifted to 1.50 eV due to the dominant contribution of SnIP in photon absorption pattern (Figure 3b).

All devices were subject to extensive characterization. Adding SnIP to CNFCl does not significantly change the resistivity (Figure 3c) of the thin film device and SnIP remained crystalline after the fabrication process (cf. Figure 3e). The XRD diffractogram of CNFCl display a broad reflection at 2θ values $\approx 27.1^\circ$ corresponded to (002) planes with a 0.33 nm interlayer d than that reported for pristine g - C_3N_4 (0.32 nm) which was assumed to be due to increased repulsion owing to out-of-plane F atoms. SnIP exhibits various XRD reflections at 2θ values of $24.1^\circ, 27.4^\circ, 29.1^\circ, 30.4^\circ, 31.6^\circ, 32.3^\circ, 34.1^\circ, 40.1^\circ,$ and 44.5° in excellent agreement with the previous literature. On mixing and wrapping CNFCl around the SnIP nanorod structure, as the wt% of SnIP in the blend is increased, the peak at $\approx 27.1^\circ$ for CNFCl weakens and the peaks of SnIP begin to strengthen in intensity. Steady state PL spectra (Figure S16, Supporting Information) of CNFCl show an intense and broad PL peak at centered at 481 nm, which is indicative of radiative recombination process of photogenerated charge carriers. For SnIP the PL peak intensity was extremely small. After coating of CNFCl on SnIP nanorod structure, the PL intensity of CNFCl was decreased significantly which was assumed due to efficient charge separation process. Further to investigate nature of charge carrier recombination processes and their lifetime, we have performed time resolved photoluminescence lifetime (TRPL) measurement by using 405 nm excitation laser. The PL decay curve of the CNFCl and SnIP can be fitted triexponentially using following equation

$$I(t) = A_1e^{-t/\tau_1} + A_2e^{-t/\tau_2} + A_3e^{-t/\tau_3} \quad (1)$$

where, $A_1, A_2,$ and A_3 represent normalized percentage of each decay components and $\tau_1, \tau_2,$ and τ_3 are e lifetime of each decay components respectively. The presence of three PL lifetime decay components in PL lifetime decay curve of CNFCl was in good agreement with previously reported literature and originated due to interband π^* - π , π^* -LP and trap assisted recombination within sheets respectively.^[30,31] The effective lifetime (τ_{eff}) which is more accurate and rational measure

of charge carrier separability was calculated using following expression.

$$\tau_{\text{eff}} = (A_1\tau_1^2 + A_2\tau_2^2 + A_3\tau_3^2) / (A_1\tau_1 + A_2\tau_2 + A_3\tau_3) \quad (2)$$

The average lifetimes of CNFCl, 10% SnIP/CNFCl, 20% SnIP/CNFCl, 30% SnIP/CNFCl, and 70% SnIP/CNFCl were found to be 4.57, 4.85, 4.67, 4.77, and 4.54 ns respectively, which revealed an efficient charge separation process, which was assumed to occur due to efficient coating and breaking of interlayer hydrogen bonding between the wrapped CNFCl sheets.^[32]

2.4. Application of SnIP Hybrids

The beneficial properties explained above encouraged us to measure the activity of the SnIP@CNFCl hybrids in photoelectrochemical water splitting. By themselves, SnIP and CNFCl are subject to severe leaching in aqueous electrolytes and the photoelectrochemical performance of each is very poor due to leaching and charge transfer problems (Figure 3f,g). However, the SnIP@CNFCl hybrids displayed very promising photoelectrochemical performance (Figures 3f,3g) and extended durability of the photoresponse (Figure 3f). The photocurrent density of pristine SnIP was found to be $23 \mu\text{A cm}^{-2}$ during on-off cycle. The light response was checked for bare $C_3N_4(\text{F,Cl})$ as well as selected SnIP@ $C_3N_4(\text{F,Cl})$ hybrid devices, as shown in Figure 3f. While $C_3N_4(\text{F,Cl})$ and the SnIP/ $C_3N_4(\text{F,Cl})_{70}$ sample show almost the same current density of 160 – $170 \mu\text{A cm}^{-2}$ in on/off measurements, an optimized ratio of the two components in SnIP/ $C_3N_4(\text{F,Cl})_{30}$ led to a significant almost fourfold improvement resulting in a current density of 0.6 mA cm^{-2} . Such a remarkable improvement in both the photoelectrochemical stability and photoelectrochemical performance of the SnIP@CNFCl hybrids over the stand-alone SnIP and CNFCl photoanodes stimulated further characterization to understand the structure of the heterojunction.

To elucidate the energy level alignment in the hybrids, Mott-Schottky measurements were performed in $0.5 \text{ M Na}_2\text{SO}_4$ solution (Figure 3h). The flat band positions from Mott-Schottky plot for bare SnIP, CNFCl, 30% SnIP/CNFCl, and 70% CNFCl were found to be at $-0.15, -0.28, -0.24,$ and -0.07 V versus Ag/AgCl, respectively. The wrapping of CNFCl on SnIP nanorod structures (see next paragraph) leads to n-type behavior of the hybrids. Further to determine the position of valence band (VB) X-ray photoelectron spectroscopy (XPS) spectra were collected and extrapolation of linear region on X and Y scale and point of intersection gave the position of the valence band with respect to the Fermi level. From the valence band XPS spectra (VB XPS), the valence band maxima (VB_{max}) of pristine SnIP and CNFCl were determined to be 1.19 and 2.27 eV. The value of VB_{max} for 30% SnIP/CNFCl was calculated to be 1.83 eV which was intermediate between VB_{max} of pristine CNFCl and SnIP respectively (Figure S21, Supporting Information).

To understand the performance increase for the 30% SnIP/CNFCl hybrids we investigated this material in more detail. The high resolution transmission microscopy (HRTEM)

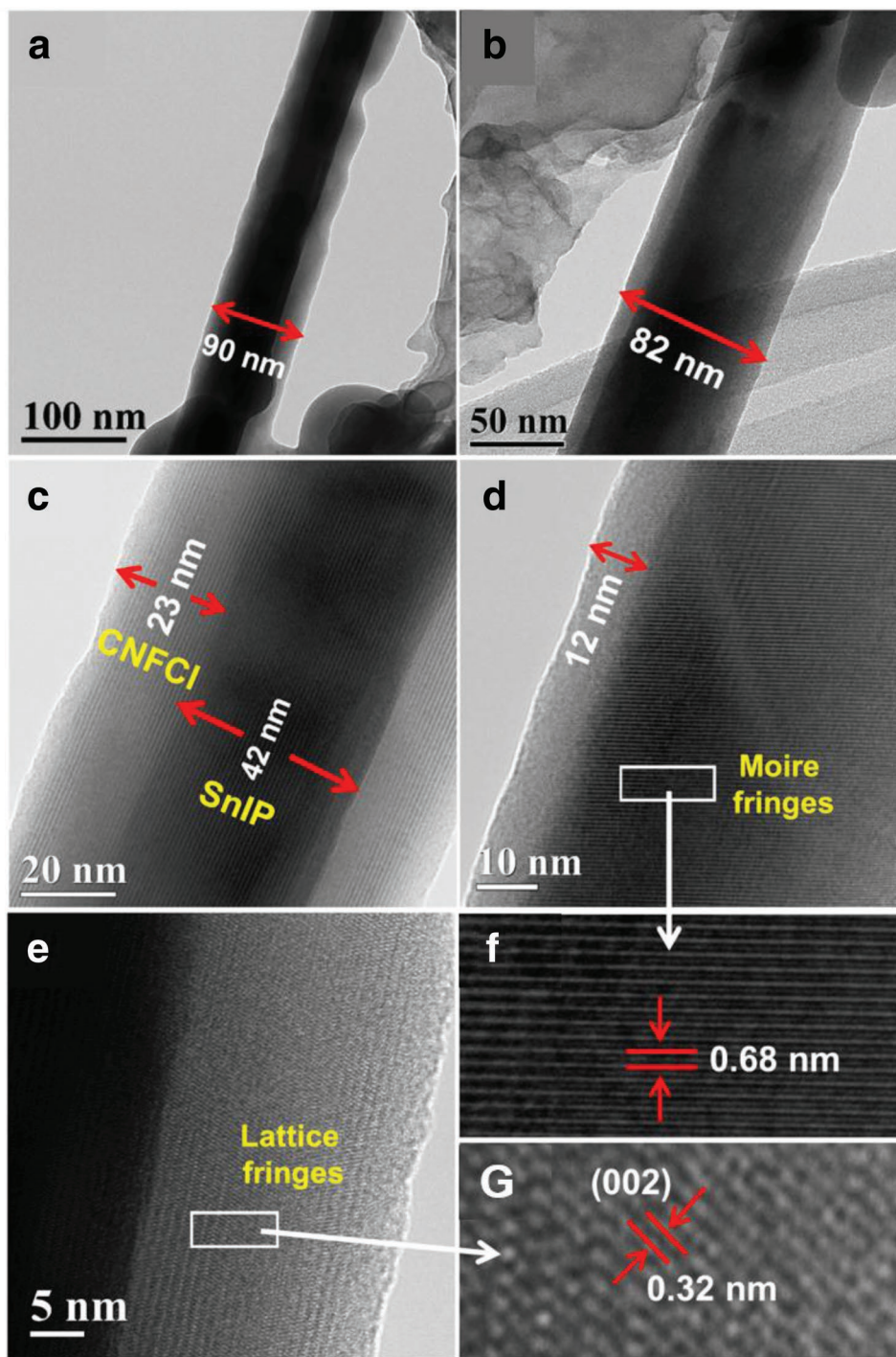


Figure 4. HRTEM images of 30% SnIP/CNFCl showing CNFCl wrapped SnIP nanorods at a,b). 100 nm scale bar showing average thickness of CNFCl enwrapped nanostructures, c) image at 20 nm scale showing inner SnIP core and CNFCl wrapped shell, d) enlarged image at 10 nm depicting Moire fringes and shell of CNFCl, e) image at 5 nm scale showing lattice fringes of CNFCl shell, f) showing zoomed view of Moire fringes and g) zoomed view of shell showing two spacing of CNFCl sheets.

image of 30% SnIP/CNFCl composite shows a clear 1D core-shell nanorod morphology with a diameter of $\approx 80\text{--}90$ nm, consisting of a dense SnIP core ($\approx 40\text{--}50$ nm) and sparse CNFCl shell wrapping the SnIP (Figure 4a–c). However, the thickness of CNFCl shell was not constant and varied from

12–25 nm. High magnification HRTEM images show higher d spacing (0.65 nm) Moire fringes (Figure 4d–f). The Moire fringes are usually observed in layered materials and originate from mismatched superimposition (dislocation or rotational) of two lattices with identical or very small difference

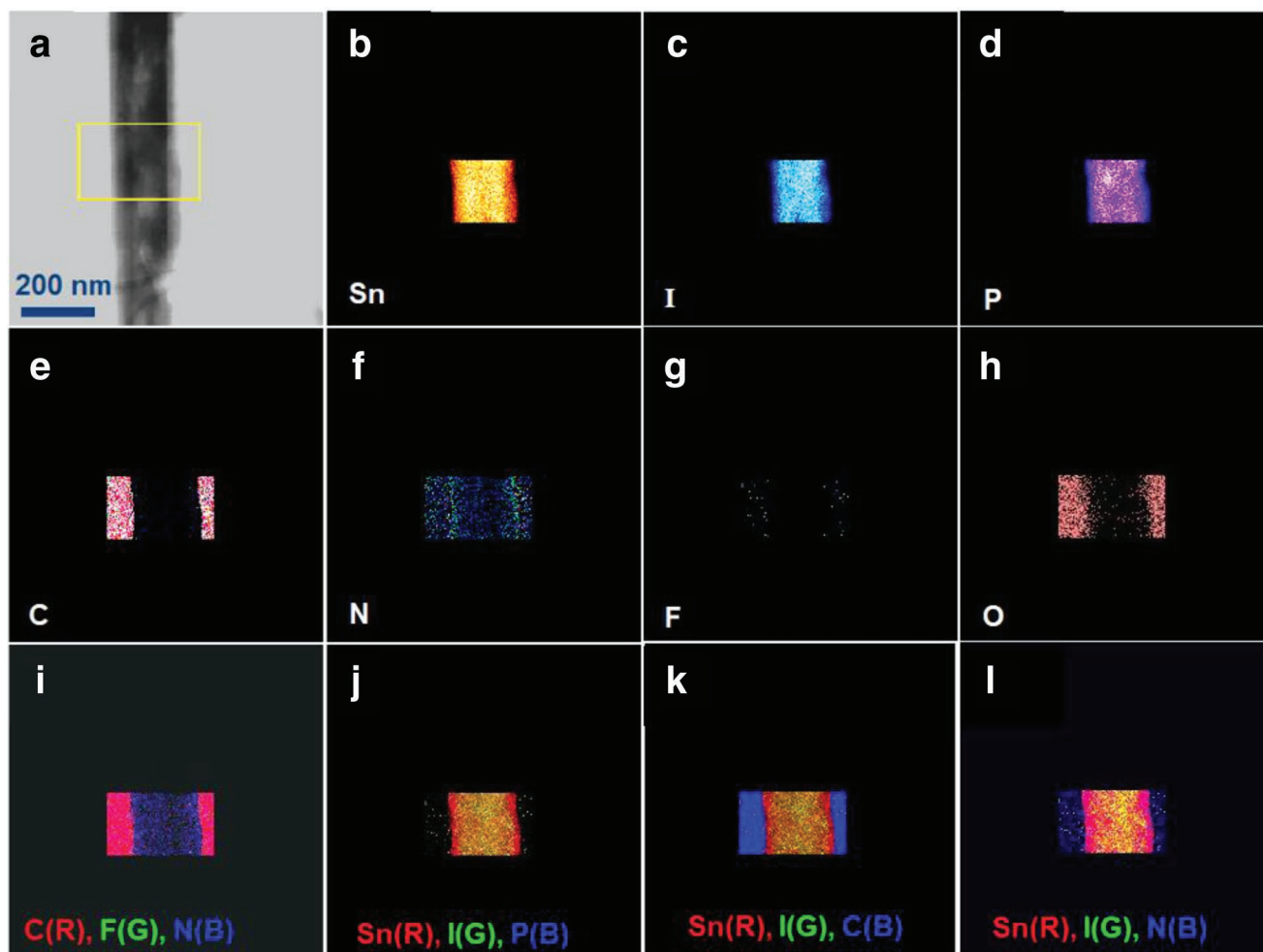


Figure 5. Scanning transmission electron microscope (STEM) elemental mapping of 30% SnIP/CNFCl a) high-angle annular dark field (HAADF) image, and mapping for b) Sn, c) I, d) P, e) C, f) N, g) F, h) O, and RGB images i) C (red), F (green), N (blue), j) Sn (red), I (green), P (blue), k) Sn (red), I (green), C (blue), l) Sn (red), I (green), and N (blue).

in d spacing. The presence of Moire fringes implicates that process of few layered CNFCl sheets folding on SnIP cores leads to lattice mismatch (probably rotational) and prevents perfect π - π stacking. Additionally, the HRTEM image at 5 nm scale bar also shows lattice fringes with smaller d spacing of 0.32 nm corroborated to (002) planes of multilayered sheets with graphitic structure. The presence of CNFCl sheets wrapped around SnIP nanorods was validated by quantitative elemental mapping which displays the relative concentration of various elements in a single core-shell nanorod measured in scanning transmission electron microscope (STEM) mode (Figure 5). Figure 5a displays the bright field electron images of 30% SnIP/CNFCl and the area of scanning. The elemental mapping of SnIP/CNFCl shows equally intense and evenly distributed concentration of Sn, I, and P in the center of scanned area confirms presence of SnIP core (Figure 5b–d) while the higher concentration of C, N, F, and O at the outer shell confirms the presence of CNFCl wrapped shell (Figure 5e–h). Further, integration of images on RGB (red, green and blue) scale to determine comparative distribution C, N and F to Sn, I and P clearly demonstrates dense SnIP core surrounded by CNFCl

shell and confirms the SnIP/CNFCl core-shell structure (Figure 5i–l). Additionally, EDX spectra of mapped area show presence of Sn, I, P, C, N, and F elements with $\approx 3:4$ C:N at% ratio, and further confirms the SnIP/CNFCl core-shell morphology (Figure S17a, Supporting Information). Elemental line scan to verify an even distribution of CNFCl over SnIP nanorod structure indeed shows an even distribution of C, N, and F with high signal intensities for Sn, I, and P at the center confirming that SnIP nanorods were efficiently covered with CNFCl sheets (Figure S17b, Supporting Information).

High resolution X-ray photoelectron spectroscopy (HRXPS) was employed to unveil the surface chemical composition (Figure 6). There was no indication of chemical bonding between SnIP and CNFCl, thus lending support to the strong interaction between the two materials being governed entirely by weaker van der Waals forces. Various peaks in the XPS survey scan of SnIP (Sn3d, I3d, P2p), CNFCl (C1s, N1s, F1s), and 30% SnIP/CNFCl (Sn3d, I3d, P2p, C1s, N1s, F1s) confirm the presence of all the relevant elements in the materials (Figure S18a, Supporting Information). The deconvoluted HRXPS spectra of pristine SnIP in Sn 3d region gave two peaks centered at

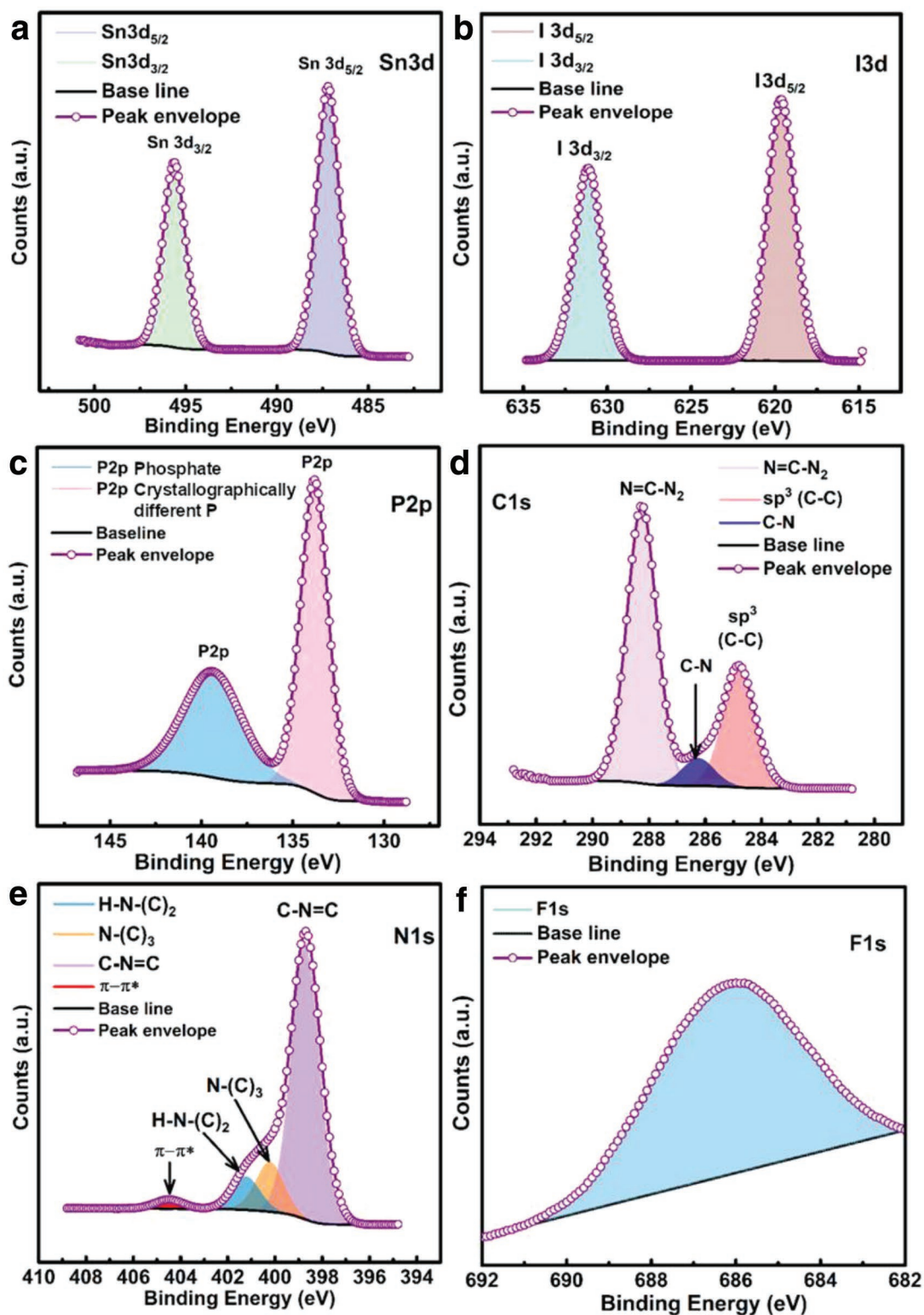


Figure 6. HRXPS core level spectra of 30% SnIP/CNFCl in a) Sn3d, b) I3d, c) P2p, d) C1s, e) N1s, and f) F1s regions.

binding energy (BE) 487.05 and 495.50 eV corroborated to Sn3d_{5/2} and Sn3d_{3/2} components which reveals the presence of chemically equivalent Sn²⁺ (Figure S18b, Supporting Information).

The HRXPS in I3d region depicted two peak components at binding energies 619.32 and 630.91 eV. While the peak in P2p region can be split into two peak components located at

133.57 eV assigned to crystallographically different P species in SnIP (Figure S18c, Supporting Information) and at 139.44 eV (caused by phosphate due to oxidation processes as reported for different phosphides in^[33–40]). The HRXPS spectrum of CNFCl in C1s region after deconvolution gave peak components located at BE values of 284.5, 286.12, and 288.12 eV assigned to adventitious and sp³ hybridized C, C–N, and N=C–N₂ carbons in g-C₃N₄.^[41] Further, deconvoluted N1s spectra show four peak components at binding energies of 398.58, 399.90, 401.17, and 404.40 eV, which were assigned to C–N=C, N–(C)₃, H–N–C₂ and π - π^* confirming a well ordered g-C₃N₄ structure.^[42] Further, F1s XPS shows one intense peak at a binding energy of 686.13 eV confirming successful doping of F atoms in the carbon nitride scaffold. Additionally, the presence of a single peak component in the O1s region at a BE value of 532.04 eV originates from surface adsorbed water and -OH moiety. The XPS spectra of 30% SnIP/CNFCl display all the peaks corresponding to SnIP and CNFCl.

3. Conclusion

SnIP has proven to be a highly flexible and stable 1D semiconductor for 1D semiconductor devices. In situ Raman spectroscopy substantiated the robustness and flexibility of SnIP upon bending, featuring an unaffected bonding within the single helices. SnIP show a comparable Young's modulus like steel along the double helix axis while the bulk modulus of bare SnIP is remarkably low, being approximately four times smaller than any state-of-the-art inorganic group IV, III-V, or II-VI semiconductors. Due to its structure, SnIP shows polymer-like behavior which is unusual for a pure inorganic material. Its structural anisotropy is also reflected in the thermal transport properties. According to DFT calculations, SnIP shows a very low and anisotropic, thermal conductivity with significantly shorter mean free pathways for phonons perpendicular than along the double helices. Heading toward the first atomic-scale chiral inorganic semiconductor, first principle calculations regarding the existence and possible formation of single SnIP double helix@CNT heterostructures were successful and reasonable metallic, semi-metallic and semiconducting CNTs were identified as possible hosts.

Based on the anisotropy of SnIP, its ability to be delaminated into small nanofibers, and the weak van der Waals bonding among SnIP double helices and to neighbored species, this material offers remarkable mechanic properties. Different important nonconductive/conductive polymers and halide-doped C₃N₄ were selected for the successful fabrication of thin-film and electrospun hybrid materials as well as 1D heterostructures. SnIP is stable in such environments and therefore defines a solid basis for future application in energy conversion and storage processes. Especially the ability of SnIP to coordinate to extended π systems offers great opportunities for functionalization and heterostructure formation with organic and inorganic compounds. 1D van der Waals type SnIP@C₃N₄(F,Cl) hybrids were tested for water splitting purposes. An almost fourfold increase of the water splitting tendency was observed for a SnIP:C₃N₄(F,Cl) 30:70 heterostructure device. Besides 3D quantum dots, the large family

of layered or so-called 2D semiconductors, strongly anisotropic 1D SnIP and its heterostructure representatives are promising candidates of a new class of flexible semiconductors with a great potential in materials science and energy related developments.

4. Experimental Section

Synthesis of SnIP: SnIP was prepared from the elements in a solid state short-way transport reaction according to the procedure described in the literature (17). 48.3 mg Tin (99.99%, VWR CHEMICALS), 16.8 mg red phosphorous (> 99.999%, CHEMPUR), and 84.9 mg SnI₄ were mixed and sealed in a silica glass ampule under vacuum ($p < 10^{-3}$ mbar). Phase pure SnI₄ was prepared according to literature.^[43]

The ampoule (length 6 cm) was placed in a NABERTHERM Muffle Furnace (L3/11/330) with the educts located close to the heating plates and the empty part of the ampoule toward in the cooler middle part of the oven. The mixture was then heated up to 673 K within 4 h, kept at this temperature for 48 h within the natural temperature gradient of the muffle furnace, and cooled down to room temperature in 120 h afterward.

Phase purity was checked prior to all following experiments by powder X-ray phase analysis and semiquantitative EDX analyses. SnIP was phase pure within the detection limit of X-ray diffraction and EDX analyses showed the expected atomic ratio of 1:1:1 for Sn:P:I. No other impurities were found.

Chemical Exfoliation of SnIP: SnIP needles were mechanically ground in an agate mortar and suspended in toluene or water. The mixture treated with an IKA T18 digital ULTRA TURRAX at 13 000 rpm for 10 min. To achieve even smaller particles the suspension was treated with a SONOPLUS ultrasonic-homogenizer from BANDELIN for 10 h. This approach yields in nanorods with diameters smaller than 25 nm. The suspension was dried under vacuum to obtain a homogeneous powder. The product was analyzed via an optical light microscope from LEICA DM 1750 M (10 × 100 magnification), powder diffraction and scanning electron microscopy.

Film Formation, Coating Methods, and Electrospinning: The different polymers were dissolved in a suitable solvent and stirred for an hour. SnIP was added to the polymer solution and stirred until a homogeneous 10:1, 1:1, or 1:10 suspension was achieved. The suspension was drop coated, spin coated, or solution casted onto a glass microscope slide and dried at room temperature. If the polymer was unstable under ambient conditions, the procedure was conducted under inert conditions, in the dark or at a reduced temperature. The homogeneity of the formed films was verified via optical light microscopy (LEICA DM 1750 M, 10 × 100 magnification) and scanning electron microscopy.

The electrospinning solution was prepared by dissolving PEO (7.95 mmol, 0.35 g) in 5 mL acetonitrile (VWR, > 99.8, H₂O < 30 ppm). After 1 h SnIP was added in a PEO:SnIP weight ratio of 10:1 or 1:1. The obtained suspension was stirred 24 h for homogenization. The whole process was performed in a flask under an argon atmosphere. Subsequently, the solution was used for electrospinning in a self-made electrospinning apparatus described elsewhere.^[44] During electrospinning a 0.9 mm (inner diameter) injector was used at a flow rate of 3.5 mL min⁻¹ and an acceleration voltage of 10.9 kV. To aim for membranes with aligned fibers, a collector consisting of two parallel, separately grounded, aluminum plates was used. The obtained membranes were dried under vacuum for 24 h prior to analysis.

Formation of SnIP–CNFCl Hybrids: For the synthesis of SnIP/CNFCl composites, 30 mg mL⁻¹ suspension of CNFCl was prepared in chlorobenzene by sonicating 4 h followed by addition of calculated wt% amount (10–90 wt%) of SnIP. The obtained mixture was sonicated for 30 min and later stirred for 24 h to get CNFCl enwrapped SnIP nanocomposite (SnIP/CNFCl). The afforded SnIP/CNFCl nanocomposite was dried by evaporating chlorobenzene. For comparison, control samples of SnIP and CNFCl was also prepared under identical conditions.

Quantum-Chemical Calculations: Pressure dependent calculations were performed in the framework of DFT using the Crystal14 code.^[45] For the contemplated elements effective core pseudopotential (ECP) and all electron valence basis sets were used.^[46] With shrinking factors of 8 and 8, creating a Pack–Monkhorst net of 170 k-points in the irreducible part of the reciprocal unit cell, delivered reliable results. The pressure was simulated by reducing the respective unit cell axis lengths in steps of 2% of the axis lengths. For a better description of the weak dispersion interactions between the double helical strands, the Grimme D2 dispersion was applied.^[47]

Phonon dispersion relations and thermal transport were computed by first-principles DFT calculations within local density approximation (LDA) of the exchange and correlation functional,^[48] using the Quantum-Espresso package.^[49] Core electrons were approximated using Projector-Augmented Wave (PAW) pseudopotentials,^[50,51] and the Kohn–Sham wave functions were expanded on a plane wave basis set with a cutoff of 60 Ry (816 eV). The charge density was integrated on $4 \times 4 \times 2$ Monkhorst–Pack meshes of k-points.^[52] The convergence thresholds for electronic self-consistent calculation and for ionic relaxation were 10^{-12} Ry and 10^{-4} Ry/au, respectively.

Harmonic second order interatomic force constants (IFCs) and phonon spectra were computed using density-functional perturbation theory (DFPT)^[53] with $4 \times 4 \times 2$ q-mesh. Anharmonic third order IFCs were computed by finite differences ($\Delta x = 0.01$ Å), in a $2 \times 2 \times 1$ a supercell containing 168 atoms, with a cutoff interaction distance up to the 6th shell of neighbors. Translational invariance of the anharmonic force constants was enforced using the Lagrangian approach.^[54] With the second and third order IFCs, the thermal conductivity of SnIP was computed by solving the phonon Boltzmann transport equation (BTE) with an iterative self-consistent algorithm, using the ShengBTE code^[54] with q-point grids up to $12 \times 12 \times 6$, considering phonon-phonon and isotopic scattering.^[55]

Ab initio calculations on SnIP@CNT heterostructures were performed using the Crystal17 code.^[56] Due to the size of the systems the GGA-level functional from Perdew, Burke, and Ernzerhof (PBE)^[57,58] was used to optimize the geometry as a 1D material. The converged structures were restarted with the HSE06 functional^[59,60] for better comparability. For contemplated elements, LCAO-basis sets with an effective core pseudopotential (ECP) and an all electron valence were chosen. With the shrinking factors of 10 and 10, a Pack–Monkhorst net^[52] was converged in the reciprocal space. The structures were optimized with (and without) assumed strong dispersion forces following the Grimme scheme.^[47] For the visualization of the structures the graphical surface of the JMOL package was used. The electronic properties (band structure, DOS, and frequency) were calculated with the Crystal17 properties setup^[56] and visualized by the CRYSPLOT online tool from the University of Torino.^[61]

Morphology, Structure, Composition, and Optical Properties: Semiquantitative elemental analyses were performed using a JOEL JCM-6000 NeoScop scanning electron microscope with an integrated JOEL JED-2200 EDS unit. The acceleration voltage was 15 kV. The measured composition was in good agreement with the nominal composition. No impurities were detected. The field emission scanning electron microscopy (FESEM) elemental mapping and energy dispersive spectrometry (EDS) was acquired on Zeiss Sigma FESEM w/EDX&EBSD integrated with Oxford AZtecSynergy system working at 15 kV acceleration voltage. The acquisition time for collecting elemental scan was 300 s. HRTEM for determining ultrafine morphological features, EDX elemental mapping, and bright field images of materials were recorded on a JEOL 2200 FS TEM/STEM equipped with STEM EDX detector, operating at an acceleration voltage of 200 keV. The samples for HRTEM were prepared by deposition of very dilute suspension of sample in methanol on a lacy carbon coated copper TEM grid followed by drying under table lamp. The system-generated dm3 HRTEM files were processed with Gatan micrograph to determine size and interplanar d spacing while elemental mapping files were processed with INCA Energy to extract 16-bit depth files and later processed in Gatan micrograph to derive RGB images. The surface chemical nature and binding energy of various elements in samples

were determined with XPS employing XPS (Axis-Ultra, Kratos Analytical) instrument endowed with monochromatic Al-K α source (15 kV, 50 W) and photon energy of 1486.7 eV under ultrahigh vacuum ($\approx 10^{-8}$ Torr). To assign the binding energy of various elements the C1s XPS peak of adventitious carbons at binding energy BE ≈ 284.8 eV was used as standard for carbon correction. Acquired raw data were deconvoluted into various peak components by using CasaXPS software and exported .csv files and plotted in origin 8.5. The crystalline features and phase structure of materials were executed with powder X-ray diffraction (XRD) recorded on Bruker D8 Discover instrument using Cu-K α radiation (40 kV, $\lambda = 0.15418$ nm) equipped with a LynxEYE 1D detector. The spectra were recorded in a range of 2θ value $20\text{--}70^\circ$ with a scan size 0.02° . The absorption properties of materials in UV–vis region were determined by diffuse reflectance UV–vis (DR UV–vis) using a Perkin Elmer Lambda-1050 UV–vis–NIR spectrophotometer equipped with an integrating sphere accessory. The steady state photoluminescence (PL) spectra to investigate photoluminescence behavior of materials were executed by using Varian Cary Eclipse fluorimeter armed with xenon lamp excitation source with a slit width of 5 nm. The PL lifetime decay curve of materials was determined with TRPL using a homemade single photon counting. A 405 nm picosecond diode laser (Alphasal GmbH) operated at a frequency of 13 MHz was used to excite the samples, and a Becker-Hickl HPM-100-50 PMT interfaced to an SPC-130 pulse counter system to collect signals. The response time of setup was ≈ 100 ps.

Raman Spectroscopy on SnIP: Raman spectra of pure SnIP and hybrids were obtained by a SENTERRA Spectrometer (BRUKEROPTICS GmbH) equipped with a 532 nm laser, between 0.1 and 1% power (1 mW) and an integration time between 30 and 250 s. The magnification was of $50\times$ (slide 50×1000 μm , zoom lens 50 long distance).

Inelastic Neutron Scattering on SnIP: High-resolution INS measurements on a 3 g powder sample in a flat aluminum cell of cross-sectional area 4×4.8 cm^2 were performed at the inverted-geometry neutron spectrometer TOSCA,^[62] spanning energy transfers up to 4000 cm^{-1} , at the ISIS Pulsed Neutron & Muon Source, Rutherford Appleton Laboratory, United Kingdom. The spectral resolution of TOSCA was similar to that of infrared and Raman techniques, being $\approx 2\%$ of the energy in question. The sample was studied at low temperature (≈ 10 K) using a dedicated closed-cycle helium refrigerator, so as to minimize the effect of the Debye Waller factor, thus allowing to fully distinguish the individual peaks. Data were reduced with the Mantid software.^[63] DFT phonon calculations were compared directly to the data from TOSCA via data processing in the software package ABINS.^[64]

High Pressure Synchrotron Experiments: All high-pressure powder X-ray experiments were performed at the beamline I15 at the Diamond Lightsource, UK with an X-ray wavelength of 25.5 keV (Ag K edge). For Diamond Anvil Cell experiments, DACs with Diamonds with 750 μm in diameter were used with Daphne oil 50 as pressure transmitting medium and ruby fluorescence as pressure calibrant. Daphne oil is known to behave hydrostatic until a pressure of approximately $p = 0.9$ GPa. However, HPXRD DAC experiments were performed in the pressure range $p =$ ambient to 4 GPa. For the DAC measurements a 2D Mythen area detector was used, of which the sample-to-detector distance was calibrated prior to the experiment with a CeO₂ standard. High-pressure experiments in the low-pressure regime between $p =$ ambient to 0.4 GPa in 250 bar steps were performed by using a self-built high-pressure cell (<https://www.imperial.ac.uk/pressurecell/>). Similar to the DAC experiments, Daphne oil 50 was used as pressure transmitting medium. In the case of these experiments, a 2D PerkinElmer detector was used and the sample-to-detector distance calibrated with using CeO₂ as standard. It should be noted that during sample loading, the sample-to-detector distance might be affected, which was taken care of in the profile fit analysis. The 2D detector files of both experiments were compiled to 1D HPPXRD data by using DAWN.

Powder Diffraction (PXRD): Phase analysis of the nanostructured SnIP powder and the obtained hybrid films was conducted using X-ray powder diffraction. The unit cell parameters were determined with the software suit STOEWINXPOW.^[65] The crystal parameters of SnIP were taken from the literature.^[17] All analyzed samples were ground in an agate

mortar, placed between two stripes of SCOTCH Magic™ 810, 3M tape and fixed onto a flat sample holder. The measurements were conducted using Cu-K α 1 radiation ($\lambda = 1.54051 \text{ \AA}$, Ge(111) monochromator) on a STOE Stadi-P powder diffraction diffractometer, equipped with a DECTRIS MYTHEN 1K detector. The measurements were conducted in a range between 5° and 90° 2θ within 15 min.

High Pressure PXRD Analysis: Profile fits of the obtained HPPXRD data were performed with TOPAS academic v5. As mentioned above, the sample-to-detector distance of the LPC possibly changes due to sample mounting. Therefore, HPPXRD data of the LPC setup was initially calibrated against the $V(p = \text{ambient})$ volume of the DAC experiments. The obtained values, and particularly the slopes of both datasets were in very good agreement (see Figure 1b in the manuscript). Additionally, attention was paid to the evolution of the full-width of half maximum (FWHM) as a function of pressure. While there was no significant change of the FWHM of the LPC experiment, an onset of increasing FWHM was found for the DAC experiments at around ≈ 1.1 GPa which was in good agreement with the reported hydrostatic limit of Daphne oil of ≈ 0.9 GPa. Furthermore, an Ff-plot (strain vs normalized pressure), points at the presence of a pressure induced phase transition in SnIP at around 0.6 GPa which was not visible by normal inspection of the PXRD pattern. Since the bulk modulus was not defined over a phase transition, only five data points from DAC experiments could be used for the analysis of the bulk modulus in the range $p < 0.6$ GPa. To obtain the bulk modulus to the highest possible accuracy, LPC experiments were performed and the bulk modulus obtained from both fitting a Birch–Murnaghan equation of state to the compiled dataset, obtaining a bulk modulus of $K = 15.45$ (with $K' = 8.21$ GPa). In order to test the accuracy of the bulk modulus against measurement errors due to different cell setups, the bulk moduli of the single measurement were also calculated to $K(\text{LPC}) = 15.1$ GPa and $K(\text{DAC}) = 16.1$ GPa. Hence, the error of the bulk modulus of was estimated to be $\approx 5\%$.

Thermal Analysis: The thermal analysis of the starting polymers and hybrid films were conducted with a NETZSCH DSC 200 F3 Maia up to a maximum of 623 K. The samples were sealed under inert conditions in an aluminum crucible. Both, the heating and cooling rate were set to 10 K min^{-1} .

Electrochemical Characterization: Mott–Schottky plot was accumulated from impedance-potential values in $0.5 \text{ M Na}_2\text{SO}_4$ in the -1.0 to $+1.0$ V voltage range at 1K frequency. Nyquist plot was prepared by electrochemical impedance spectroscopy (EIS), measured using a three electrodes configuration at applied voltage of 0 V versus Ag/AgCl in $0.1 \text{ M Na}_2\text{SO}_4$, with AC amplitude of 0.005 V at frequency value 0.1 Hz to 1000 kHz .

Photoelectrochemical Experiments: Prior to photoelectrochemical measurements, a 60 nm thick TiO_2 blocking layer was deposited on cleaned FTO glass slides by spin casting using titanium di-isopropoxide solution as precursor, and then used as the substrate for subsequent experiments. The CNFCl and various wt% SnIP/CNFCl samples were mixed with α -terpineol (film forming agent) to obtain a concentration of 30 mg mL^{-1} and stirred for 2 h. The obtained solution was drop coated onto the substrate followed by heating at 250°C for 1 h. The fabricated thin film was sealed with a Surlyn sheet keeping a 1-inch diameter circular surface exposed. The thin film on substrate was assigned as the photoanode (working electrode) in a three-electrode system water-splitting setup while Pt and Ag/AgCl were used as counter electrode (cathode) and reference electrode, respectively. The photoelectrochemical water splitting experiment was performed by immersing the electrodes in $0.1 \text{ M Na}_2\text{SO}_4$ solution. The photoanode was irradiated under simulated sunlight (AM 1.5 G) with an intensity of 100 mW cm^{-2} at the surface of the sample. Wavelengths lower than 420 nm were filtered using a UV cut off filter to ascertain the visible light response of samples. Photocurrent density versus applied voltage graph to check photoresponse of samples were determined by linear sweep voltammetry by sweeping voltage from -0.8 to $+0.8 \text{ V}$. Additionally, photoresponse at 425 and 505 nm wavelength was investigated by irradiating sample with 450 and 505 nm LEDs. The

LEDs were calibrated with a photodiode and the power density on the surface of samples were calculated to be 47.70 and 40.48 mW cm^{-2} for 425 and 505 nm LEDs respectively. For comparison, dark current was also measured.

Young's Modulus Determination: The Young's modulus was determined using a Nanoscope Dimension 3000 AFM in nanoindentation mode. 500 nm deep, about $25 \times 25 \mu\text{m}^2$ wide trenches were etched into an SiO_2 coated Si wafer via reactive ion etch using a TEM grid as shadow mask. Subsequently, SnIP wires were deposited by immersing the etched substrates into the SnIP suspension for about 10 min until the solvent (toluene) was evaporated. The samples were not rinsed off or blow-dried to prevent displacement of the wires. Suitable wires bridging etched holes were located under an optical microscope (Figures S1a and S2a, Supporting Information).

Supporting Information

Supporting Information is available from the Wiley Online Library or from the author.

Acknowledgements

C.O., F.R., and T.U.K. contributed equally to this work. The research leading to this result has been supported by the ATUMS graduate school IRTG2020 financed by Natural Sciences and Engineering Research Council of Canada (NSERC) and Deutsche Forschungsgemeinschaft (DFG), the Grant No. NI1095/8-1 by DFG, the project CALIPSO plus under the Grant Agreement 730872 from the EU Framework Programme for Research and Innovation HORIZON 2020, Germany's Excellence Strategy-EXC2089/1-390776260, and the Diamond Light Source Ltd. The authors thank the IGCSE and TUM Graduate School for continuous support. T.U.K., P.K., and K.S. would like to thank NSERC, the National Research Council Canada (NRC), Future Energy Systems (FES), and CMC Microsystems for direct and indirect (equipment uses) financial support. T.U.K. thanks Prof. Alkiviathes Meldrum for his kind help in TRPL lifetime measurement. Dr. Kai Cui is kindly acknowledged for helping in HRTEM analysis and elemental mapping. R.T.W. acknowledges funding from the initiative "Solar Technologies go Hybrid" (Soltech), the Nanosystems Initiative Munich (NIM), and the Center for Nanoscience (CeNS) for partial financial support.

Conflict of Interest

The authors declare no conflict of interest.

Keywords

1D materials, core-shell particles, hybrid materials, inorganic double helix semiconductor SnIP, water splitting

Received: January 8, 2019

Revised: February 19, 2019

Published online:

- [1] A. P. Alivisatos, *Science* **1996**, 271, 933.
- [2] J. P. Reithmaier, G. Sek, A. Löffler, C. Hofmann, S. Kuhn, S. Reitzenstein, L. V. Keldysh, V. D. Kulakovskii, T. L. Reinecke, A. Forchel, *Nature* **2004**, 432, 197.
- [3] A. K. Geim, K. S. Novoselov, *Nat. Mater.* **2007**, 6, 183.

- [4] H. Liu, A. T. Neal, Z. Zhu, Z. Luo, X. Xu, D. Tománek, P. D. Ye, *ACS Nano* **2014**, *8*, 4033.
- [5] P. Vogt, P. De Padova, C. Quaresima, J. Avila, E. Frantzeskakis, M. C. Asensio, A. Resta, B. Ealet, G. Le Lay, *Phys. Rev. Lett.* **2012**, *108*, 155501.
- [6] D. Jose, A. Datta, *Acc. Chem. Res.* **2014**, *47*, 593.
- [7] M. M. Ugeda, A. J. Bradley, S.-F. Shi, F. H. da Jornada, Y. Zhang, D. Y. Qiu, W. Ruan, S.-K. Mo, Z. Hussain, Z.-X. Shen, F. Wang, S. G. Louie, M. F. Crommie, *Nat. Mater.* **2014**, *13*, 1091.
- [8] S. Manzeli, D. Ovchinnikov, D. Pasquier, O. V. Yazyev, A. Kis, *Nat. Rev. Mater.* **2017**, *2*, 17033.
- [9] L. Li, Y. Yu, G. J. Ye, Q. Ge, X. Ou, H. Wu, D. Feng, X. H. Chen, Y. Zhang, *Nat. Nanotechnol.* **2014**, *9*, 372.
- [10] L. Tao, E. Cinquanta, D. Chiappe, C. Grazianetti, M. Fanciulli, M. Dubey, A. Molle, D. Akinwande, *Nat. Nanotechnol.* **2015**, *10*, 227.
- [11] X. Shi, H. Chen, F. Hao, R. Liu, T. Wang, P. Qiu, U. Burkhardt, Y. Grin, L. Chen, *Nat. Mater.* **2018**, *17*, 421.
- [12] A. K. Geim, I. V. Grigorieva, *Nature* **2013**, *499*, 419.
- [13] H.-H. Fang, F. Wang, S. Adjokatse, N. Zhao, J. Even, M. A. Loi, *Light: Sci. Appl.* **2016**, *5*, e16056.
- [14] P. Liu, A. T. Liu, D. Kozawa, J. Dong, J. F. Yang, V. B. Koman, M. Saccone, S. Wang, Y. Son, M. H. Wong, M. S. Strano, *Nat. Mater.* **2018**, *17*, 1005.
- [15] H. Wang, L. A. Zepeda-Ruiz, G. H. Gilmer, M. Upmanyu, *Nat. Commun.* **2013**, *4*, 1956.
- [16] Y.-C. Chou, K. Hillerich, J. Tersoff, M. C. Reuter, K. A. Dick, F. M. Ross, *Science* **2014**, *343*, 281.
- [17] Y. Yue, Q. Zhang, Z. Yang, Q. Gong, L. Guo, *Small* **2016**, *12*, 3503.
- [18] D. Pfister, K. Schäfer, C. Ott, B. Gerke, R. Pöttgen, O. Janka, M. Baumgartner, A. Efimova, A. Hohmann, P. Schmidt, S. Venkatachalam, L. van Wüllen, U. Schürmann, L. Kienle, V. Duppel, E. Parzinger, B. Miller, J. Becker, A. Holleitner, R. Wehrich, T. Nilges, *Adv. Mater.* **2016**, *28*, 9783.
- [19] U. Müller, *Acta Crystallog., Sect. B: Struct. Sci., Cryst. Eng. Mater.* **2017**, *73*, 443.
- [20] M. Baumgartner, R. Wehrich, T. Nilges, *Chem. - Eur. J.* **2017**, *23*, 6452.
- [21] X. Li, Y. Dai, Y. Ma, M. Li, L. Yu, B. Huang, *J. Mater. Chem. A* **2017**, *5*, 8484.
- [22] S. Dissegna, P. Vervoorts, C. L. Hobday, T. Düren, D. Daisenberger, A. J. Smith, R. A. Fischer, G. Kieslich, *J. Am. Chem. Soc.* **2018**, *140*, 11581.
- [23] S. Adachi, *Properties of Group IV, III-V and II-VI Semiconductors*, John Wiley & Sons, Chichester, UK **2005**, p. 55.
- [24] Z. Chen, U. Ghandi, J. Lee, R. H. Wagoner, *J. Mater. Process. Technol.* **2016**, *227*, 227.
- [25] J. Zhang, D. Zhao, D. Xiao, C. Ma, H. Du, X. Li, L. Zhang, J. Huang, H. Huang, C. L. Jia, D. Tománek, C. Niu, *Angew. Chem., Int. Ed.* **2017**, *56*, 1850.
- [26] M. Hart, E. R. White, J. Chen, C. M. McGilvery, C. J. Pickard, A. Michaelides, A. Sella, M. S. P. Shaffer, C. G. Salzmann, *Angew. Chem., Int. Ed.* **2017**, *56*, 8144.
- [27] T. Fujimori, R. Batista dos Santos, T. Hayashi, M. Endo, K. Kaneko, D. Tománek, *ACS Nano* **2013**, *7*, 5607.
- [28] G. Chang, B. J. Wieder, F. Schindler, D. S. Sanchez, I. Belopolski, S.-M. Huang, B. Singh, D. Wu, T.-R. Chang, T. Neupert, S.-Y. Xu, H. Lin, M. Z. Hasan, *Nat. Mater.* **2018**, *17*, 978.
- [29] Y. Wang, Y. Di, M. Antonietti, H. Li, X. Chen, X. Wang, *Chem. Mater.* **2010**, *22*, 5119.
- [30] P. Yang, H. Ou, Y. Fang, X. Wang, *Angew. Chem.* **2017**, *129*, 4050.
- [31] Y. Kang, Y. Yang, L.-C. Yin, X. Kang, L. Wang, G. Liu, H.-M. Cheng, *Adv. Mater.* **2016**, *28*, 6471.
- [32] Y. Kang, Y. Yang, L.-C. Yin, X. Kang, G. Liu, H.-M. Cheng, *Adv. Mater.* **2015**, *27*, 4572.
- [33] X. Wang, W. Li, D. Xiong, D. Y. Petrovykh, L. Liu, *Adv. Funct. Mater.* **2016**, *26*, 4067.
- [34] J. Xu, J. P. S. Sousa, N. E. Mordvinova, J. D. Costa, D. Y. Petrovykh, K. Kovnir, O. I. Lebedev, Y. V. Kolen'ko, *ACS Catal.* **2018**, *8*, 2595.
- [35] T. I. Korányi, *Appl. Catal., A* **2003**, *239*, 253.
- [36] B. P. Payne, M. C. Biesinger, N. S. McIntyre, *J. Electron Spectrosc. Relat. Phenom.* **2012**, *185*, 159.
- [37] A. P. Grosvenor, S. D. Wik, R. G. Cavell, A. Mar, *Inorg. Chem.* **2005**, *44*, 8988.
- [38] P. E. R. Blanchard, A. P. Grosvenor, R. G. Cavell, A. Mar, *Chem. Mater.* **2008**, *20*, 7081.
- [39] L. Zhou, M. Shao, J. Li, S. Jiang, M. Wei, X. Duan, *Nano Energy* **2017**, *41*, 583.
- [40] Y. Pan, Y. Liu, C. Liu, *J. Power Sources* **2015**, *285*, 169.
- [41] H. Yu, R. Shi, Y. Zhao, T. Bian, Y. Zhao, C. Zhou, G. I. N. Waterhouse, L.-Z. Wu, C.-H. Tung, T. Zhang, *Adv. Mater.* **2017**, *29*, 1605148.
- [42] J. Fang, H. Fan, M. Li, C. Long, *J. Mater. Chem. A* **2015**, *3*, 13819.
- [43] M. Köpf, N. Eckstein, D. Pfister, C. Grotz, I. Krüger, M. Greiwe, T. Hansen, H. Kohlmann, T. Nilges, *J. Cryst. Growth* **2014**, *405*, 6.
- [44] K. M. Freitag, H. Kirchhain, L. van Wüllen, Tom Nilges, *Inorg. Chem.* **2017**, *56*, 2100.
- [45] R. Dovesi, R. Orlando, A. Erba, C. M. Zicovich-Wilson, B. Civalleri, S. Casassa, L. Maschio, M. Ferrabone, M. De La Pierre, P. D'Arco, Y. Noël, M. Causà, M. Rérat, B. Kirtman, *Int. J. Quantum Chem.* **2014**, *114*, 1287.
- [46] F. Pascale, C. M. Zicovich-Wilson, R. Orlando, C. Roetti, P. Ugliengo, R. Dovesi, *J. Phys. Chem. B* **2005**, *109*, 6146.
- [47] S. Grimme, *J. Comput. Chem.* **2006**, *27*, 1787.
- [48] J. P. Perdew, A. Zunger, *Phys. Rev. B* **1981**, *23*, 5048.
- [49] P. Giannozzi, S. Baroni, N. Bonini, M. Calandra, R. Car, C. Cavazzoni, D. Ceresoli, G. L. Chiarotti, M. Cococcioni, I. Dabo, A. Dal Corso, S. de Gironcoli, S. Fabris, G. Fratesi, R. Gebauer, U. Gerstmann, C. Gougoussis, A. Kokalj, M. Lazzeri, L. Martin-Samos, N. Marzari, F. Mauri, R. Mazzarello, S. Paolini, A. Pasquarello, L. Paulatto, C. Sbraccia, S. Scandolo, G. Sclauzero, A. P. Seitsonen, A. Smogunov, P. Umari, R. M. Wentzcovitch, *J. Phys.: Condens. Matter* **2009**, *21*, 395502.
- [50] P. E. Blöchl, *Phys. Rev. B* **1994**, *50*, 17953.
- [51] G. Kresse, D. Joubert, *Phys. Rev. B* **1999**, *59*, 1758.
- [52] H. J. Monkhorst, J. D. Pack, *Phys. Rev. B* **1976**, *13*, 5188.
- [53] S. Baroni, S. De Gironcoli, A. Dal Corso, P. Giannozzi, *Rev. Mod. Phys.* **2001**, *73*, 515.
- [54] W. Li, J. Carrete, N. A. Katcho, N. Mingo, *Comput. Phys. Commun.* **2014**, *185*, 1747.
- [55] S.-I. Tamura, *Phys. Rev. B* **1983**, *27*, 858.
- [56] R. Dovesi, C. Roetti, R. Orlando, C. M. Zicovich-Wilson, F. Pascale, B. Civalleri, K. Doll, N. M. Harrison, I. J. Bush, P. D'Arco, M. Llunell, M. Causà, Y. Noël, L. Maschio, A. Erba, M. Rerat, S. Casassa, *CRYSTAL 17 User's Manual*: University of Torino.
- [57] J. P. Perdew, K. Burke, M. Ernzerhof, *Phys. Rev. Lett.* **1996**, *77*, 3865.
- [58] J. Paier, R. Hirschl, M. Marsman, G. Kresse, *J. Chem. Phys.* **2005**, *122*, 234102.
- [59] A. V. Krukau, G. E. Scuseria, J. P. Perdew, A. Savin, *J. Chem. Phys.* **2008**, *129*, 124103.
- [60] J. Heyd, G. E. Scuseria, M. Ernzerhof, *J. Chem. Phys.* **2006**, *124*, 219906.
- [61] CRYSPLOT, <http://crysplot.crystalsolutions.eu/> (accessed: December 2016).
- [62] R. S. Pinna, S. Rudić, S. F. Parker, J. Armstrong, M. Zanetti, G. Škoro, S. P. Waller, D. Zacek, C. A. Smith, M. J. Capstick,

- D. J. McPhail, D. E. Pooley, G. D. Howells, G. Gorini, F. Fernandez-Alonso, *Nucl. Instrum. Methods Phys. Res., Sect. A* **2018**, 896, 68.
- [63] O. Arnold, J. C. Bilheux, J. M. Borreguero, A. Buts, S. I. Campbell, L. Chapon, M. Doucet, N. Draper, R. Ferraz Leal, M. A. Gigg, V. E. Lynch, A. Markvardsen, D. J. Mikkelsen, R. L. Mikkelsen, R. Miller, K. Palmen, P. Parker, G. Passos, T. G. Perring, P. F. Peterson, S. Ren, M. A. Reuter, A. T. Savici, J. W. Taylor, R. J. Taylor, R. Tolchenov, W. Zhou, J. Zikovskiy, *Nucl. Instrum. Methods Phys. Res., Sect. A* **2014**, 764, 156.
- [64] K. Dymkowski, S. F. Parker, F. Fernandez-Alonso, S. Mukhopadhyay, *Phys. B: Condensed Matter* **2018**, 551, 443.
- [65] WinX^{POW} Software, Stoe & Cie GmbH, Darmstadt, Germany, Version 3.0.2.1, **2011**.